ACS OMEGA

http://pubs.acs.org/journal/acsodf

Article

Biocompatible and Printable Ionotronic Sensing Materials Based on Silk Fibroin and Soluble Plant-Derived Polyphenols

Irene Chiesa, Carmelo De Maria, Rodolfo Tonin, Francesca Ripanti, Maria Rachele Ceccarini, Carlotta Salvatori, Lorenzo Mussolin, Alessandro Paciaroni, Caterina Petrillo, Emanuele Cesprini, Federica Feo, Martino Calamai, Amelia Morrone, Antonino Morabito, Tommaso Beccari, and Luca Valentini*

Cite This: *ACS Omega* 2022, 7, 43729−43737

Read Online

ACCESS | Metrics & More | Article Recommendations | Supporting Information

ABSTRACT: The emergence of ionotronic materials has been recently exploited for interfacing electronics and biological tissues, improving sensing with the surrounding environment. In this paper, we investigated the synergistic effect of regenerated silk fibroin (RS) with a plant-derived polyphenol (*i.e.*, chestnut tannin) on ionic conductivity and how water molecules play critical roles in regulating ion mobility in these materials. In particular, we observed that adding tannin to RS increases the ionic conductivity, and this phenomenon is accentuated by increasing the hydration. We also demonstrated how silk-based hybrids could be used as building materials for scaffolds where human fibroblast and neural progenitor cells can highly proliferate. Finally, after proving their biocompatibility, RS hybrids demonstrate excellent three-dimensional (3D) printability via extrusion-based 3D printing to fabricate a soft sensor that can detect charged objects by sensing the electric fields that originate from them. These findings pave the way for a viable option for cell culture and novel sensors, with the potential base for tissue engineering and health monitoring.

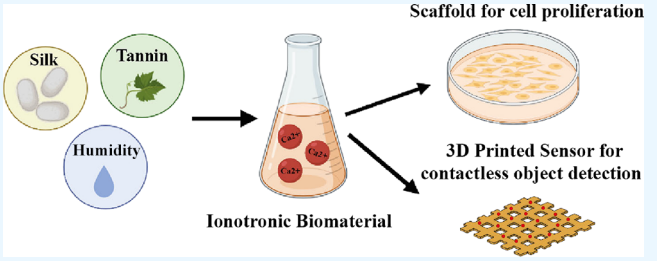

1. INTRODUCTION

Mimicking the sensing mechanisms of some animals that use electroreceptors on their skin to catch prey without physical contact,[1−3] ionotronic materials can be designed to sense a variety of stimuli, such as check noncontact spatial perception.[4−6]

Regenerated silk is a biopolymer derived from *Bombyx mori* with tunable processability and physical properties, whose unique advantages rely on biocompatibility, biodegradability, and bioabsorption,[7−10] as well as ionic conductivity due to the presence of Ca^{2+} ions that have strong capability to capture water molecules.[11,12] These merits promote regenerated silk fibroin (RS) as a biocompatible ionotronic material.

Among the plant-derived polyphenols, tannins offer important renewable resources due to their relative abundance, ease and sustainability of the extraction process, and their good reactivity.[13,14] Tannins can be divided into two main classes, condensed and hydrolyzable, which have different chemical structures and, thus, properties.[15] In the current research, we focused our attention on hydrolyzable chestnut extract for its abundance at the national level (Italy) as well as for the higher antioxidant properties of hydrolyzable tannin than the condensed one.[16]

Tannins are the second natural resource of polyphenols behind only lignin,[14] which would be an interesting resource for this kind of application. On the other hand, although research is looking for useful ways to exploit lignin, industrially, it is not yet possible to rely on raw lignin for value-added application.[17] Indeed, the high heterogeneity due to the origin and extraction method limits the industrial development,[17] and nowadays, most of the raw material is still directly burnt.[18]

Notably, the coassembly of tannins with proteins has been considered a facile method for developing a bioinspired RS-based hydrogel sealant.[19] In this regard, stimuli-responsive conductive hydrogels have been exploited as sensors for health monitoring, biocompatible electronic devices, and wound healing in tissue engineering.[20−22] Our previous work observed that tannins play a crucial role in the one-step method to generate an elastomer-like material based only on RS and calcium chloride ($CaCl_2$).[23]

Such materials present adequate mechanical properties to follow the displacement and deformation of soft biological tissues, when shaped in holey structures, as we previously showed.[24]

Received: July 27, 2022
Accepted: November 9, 2022
Published: November 28, 2022

In this work, inspired by ion electronics, Ca^{2+}-tannin-RS films (RS/T), with different tannin concentrations, were prepared via $CaCl_2$ dissolution of degummed silk and the subsequent addition of tannin. The introduction of tannin to Ca^{2+}-RS films endowed the sample with higher ionic conductivity. More importantly, these solutions were used as biomaterial ink for 3D-printing multilayered grid-like sensors that could detect the spatial localization of charged objects. We report as a proof of concept on using such 3D-printed sensors to detect the bioelectrical activity of live microorganisms. Finally, we developed a process based on such hybrid RS protein, which can self-assemble into biocompatible scaffolds at room temperature. This biobased method can provide a valuable environment for cell culture as an alternative to Matrigel, severely limited by the variability in its composition and the presence of xenogenic contaminants.[25−27] Mimicking the conduction mechanism of organs by conducting electricity via ions trapped inside,[28,29] hybrid RS promotes the differentiation and proliferation of fibroblasts and neural progenitor cells (NPCs) at rates that match its use in biomedical implants.

2. MATERIALS AND METHODS

2.1. Materials. Silk cocoons were supplied by a local farm (Fimo srl, Milano, Italy). Sodium hydrogen carbonate ($NaHCO_3$), $CaCl_2$, and formic acid (FA) were provided by Merck (Darmstadt, Germany). Commercial chestnut tannin extract "Saviota A" was kindly provided by SavioLife (Viadana, Italy).

2.2. Synthesis of RS/T Films. *B. mori* silk cocoons (10 g) were boiled for 30 min in 200 mL of water containing 5 g of $NaHCO_3$. The extract fibers were washed two times with water and dried at room temperature under a chemical hood in laminar flow. Subsequently, the fibroin fibers were dissolved in 5 mL of FA containing an amount of $CaCl_2$ equal to 90:10, 80:20, and 60:40 concerning the weight of the dried fibroin fibers (*i.e.*, 0.65 g) at 30 °C for 1 h (*i.e.*, 0.072, 0.087, and 0.43 g, respectively). Afterward, concerning the silk content, 1, 2, and 5 wt % tannins were added to the solution, respectively, leaving the dissolution to proceed at 50 °C. Films were then fabricated by drop-casting the solutions into Petri dishes with a diameter of 5 cm and left to evaporate at 40 °C for 4 h. From now on, RS/T is used for samples obtained by adding tannin, namely, RS/T1, RS/T2, and RS/T5, which refer to 1, 2, and 5 wt % tannins, respectively.

2.3. Materials Characterization. XRD measurements (Cu Kα radiation, λ = 1.5408 Å) were performed using a thin aluminum sample holder at room temperature. The scattering angle was varied in steps of $\Delta 2\theta$ = 0.2° over 2θ = 4−60° angular range, corresponding to an exchanged wavevector Q interval going from 0.57 to 7 $Å^{-1}$. The sample was tilted at ϕ = 30° angle concerning the incident radiation. An angular resolution of $\Delta 2\theta$ = 0.77° was achieved, corresponding to about ΔQ = 0.047 $Å^{-1}$ in all the investigated angular ranges. Experimental data were corrected for the sample holder, including the aluminum Bragg peak and environmental contributions.

FTIR investigations on RS and RS/T samples were carried out using a PerkinElmer spectrometer in ATR mode. Measurements were performed with a resolution of 4 cm^{-1}, and the number of scans was 200 for each spectrum. The background spectra were recorded before each spectrum. The spectra were then deconvoluted by subtracting a linear baseline and applying a Gaussian deconvoluting curve by Origin 9 software. The measurements were performed at room temperature. The spectra, the amide I and amide II bands, were collected in the range of 1750 to 1450 cm^{-1}. The secondary protein structure content was determined by fitting peaks that were assigned[30] to side chains (1605−1616 cm^{-1}), β-sheets (1616−1622, 1622−1628, 1628−1638, and 1697−1704 cm^{-1}), random coils (1638−1647 and 1647−1656 cm^{-1}), α-helices (1656−1663 cm^{-1}), and turns (1663−1671, 1671−1686, and 1686−1697 cm^{-1}). The secondary structure proportions were quantified by the ratio of the respective subpeak integrals to the total integral. The peaks related to C−C and C═O from tannin were eliminated to calculate the composition of secondary structures of silk fibroin.

RS and RS/T rectangular samples (length: 15 mm; width: 10 mm) were fixed on a Teflon substrate with two stripes of adhesive copper. The conductivity was extrapolated from the current−voltage (I−V) curve recorded by a Keithley 4200 SCS. The samples were then conditioned in a climatic chamber at different relative humidity values (RH; *i.e.*, from 0%RH to 80%RH) at 25 °C to monitor the effect of water absorption on ionic conductivity. The conductivity at −15 and 25 °C was calculated from the current−voltage (I−V) curve (Figure S1) recorded by a Keithley 4200 SCS. To evaluate the temperature response ability, the current variation was observed at −15 and 25 °C. To assess the biodegradation of the films, the samples were solubilized using a 10 mM PBS solution with pH 6.5. The solvent was added not directly onto the samples but next to them. The pH of the solution was measured before the experiment and after it was added to the wells, and they both showed the same correct pH level.

2.4. Cytotoxicity Assay In Vitro. Caco-2, a human colon adenocarcinoma cell line, was purchased directly from ATCC (Manassas, VA). Caco-2 cells were tested for mycoplasma contamination by real-time PCR before use. Cells were maintained at 37 °C in Dulbecco's modified Eagle medium (DMEM) containing 10% fetal bovine serum (FBS), 1% nonessential amino acids (NEAA), 2 mM L-glutamine, and antibiotics (100 U/mL penicillin and 100 μg/mL streptomycin) in an atmosphere of 5% CO_2 and 90%RH. In a previous paper,[24] the absence of cytotoxic effect for RS and RS/T films with 1 and 10% tannins was already proved; therefore, they were not tested, and only the new tannin concentrations (*i.e.*, 2 and 5% tannins) were investigated. RS and RS/T cytotoxicity were evaluated using the 3-(4,5-dimethylthiazol-2-yl)-2,5-diphenyltetrazolium bromide (MTT) method. Each stock solution was prepared by incubating the silk-based solution (1 mg/mL) with a complete medium (DMEM) for 1 h at 37 °C. Eight scalar dilutions from 7.8 μg/mL to 1.0 mg/mL were tested after 24 and 48 h of incubation. Optical density (OD) values were measured spectrophotometrically at 570 nm (Eliza MAT 2000, DRG Instruments GmbH, Marburg, Germany). All values were corrected for the background (*i.e.*, incubation media plus MTT without cells), and cell viability was calculated as previously reported.[31] Each experiment was performed in triplicate, and cell viability was expressed as a relative percentage, as previously described.[32]

2.5. Cell Culture and Analysis of Cells within Silk Scaffolds. RS and RS/T films were sterilized after 1 h of exposure to ultraviolet light (UV-C) in a Biosafety Level 2 cabinet. Then, films (0.04 g) were dissolved in 1 mL of DMEM using a thermomixer for 1 h at 37 °C and 1400 rpm.

The dissolved RS hybrid films were deposited onto 13 mm cover glasses (VWR) and left overnight at room temperature.

https://doi.org/10.1021/acsomega.2c04729
ACS Omega 2022, 7, 43729−43737

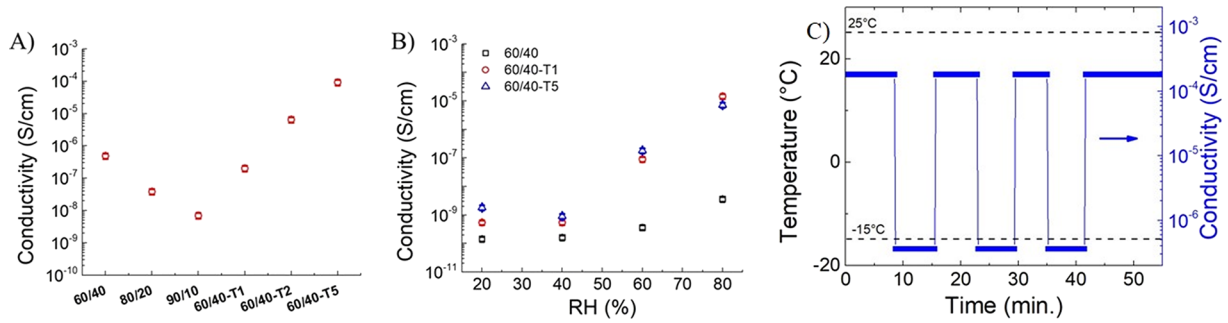

Figure 1. Evaluation of the relative humidity and temperature on the ionic conductivity of the prepared samples. (A) The ionic conductivity of RS films with different RS/$CaCl_2$ weight ratios and 60/40 RS with additional tannin content was measured at 25 °C and environmental humidity (*i.e.*, 50%RH). (B) Conductivity−humidity curve of 60/40 RS, 60/40 RS/T1, and 60/40 RS/T5. (C) Conductivity changes of the 60/40 RS/T5 film at 25 and −15 °C.

After silk sedimentation with the consistency of a gel, the excess DMEM was removed, and the RS hybrid film-modified glass surfaces were dried at room temperature to allow any DMEM residual to evaporate at least for 2 h under sterile conditions.

To monitor the gelation process and determine gelation time, turbidity changes at 550 nm were recorded.[34] Gelation was conducted in covered four-well plates (MICROTEST 96, Falcon, USA) and incubated in a light-free environment at room temperature. The microstructure change of fibroin solutions causes light scattering in the visible light range, increasing turbidity. The OD change was measured in the absorbance mode (550 nm). The gelation degree was defined as $(OD_0 - OD_t)/OD_0$, where OD_t is the optical density measured at a certain time, and OD_0 is the optical density measured at t = 0 h. FTIR measurements and analysis were also repeated for these samples.

A cell number of 3×10^4 human skin fibroblasts and iPSc-derived NPCs were seeded on silk-modified glass surfaces and grown at 37 °C in a 5% CO_2 incubator for 7 days. Fibroblasts were cultured using DMEM supplied with antibiotics and FBS (10%). NPCs were cultured using STEMdiff Neural Progenitor Medium (STEMCELL Technologies). Fibroblast and NPC morphology, growth, and confluence were evaluated daily by an inverted microscope.

After 7 days, modified glass surfaces incubated with cells were washed with PBS and fixed using 4% paraformaldehyde (PFA). After rinsing with PBS and blocking with 4% bovine serum albumin (BSA) in PBS, the samples were fluorescently labeled after simultaneous incubation for 15 min with Hoechst 33342 (Thermo Fisher) at a concentration of 1 μg/mL and with Wheat Germ Agglutinin 568 (WGA568, Thermo Fisher) at 5 μg/mL. Imaging was performed with a confocal microscope (Nikon Eclipse TE300) equipped with the Nikon C2 scanning head Coherent CUBE (diode 405 nm) and Coherent Sapphire (Sapphire 561 nm) lasers. Emission filters for imaging were 452/45 and 595/60 nm to evaluate cell adhesion and proliferation. Anonymous skin fibroblast cell lines were used in compliance with the ethical recommendations and the International Declaration on Human Genetic Data of 2003.

2.6. 3D Printing Process. Multilayered 1.5 cm × 1.5 cm × 200 μm grid structures with a 15% infill density were 3D-printed via extrusion-based 3D printing using the RS, RS/T1, and RS/T5 solutions (with a $CaCl_2$ ratio equal to 60:40), as previously described.[24] Briefly, the printing process occurred onto a water-soluble polymer layer (2 mg/mL of Hydrofilm, Lucart, Italy) attached to an acetate foil. After printing, the structures were dried at room temperature for 24 h to allow any FA residual to evaporate. Finally, the RS-based grids, still attached to the Hydrofilm layer, were peeled from the acetate foil and stored at room temperature until further use.

2.7. Proofs of Concept. The 3D-printed grids, still attached to Hydrofilm, were placed on the top of a Teflon substrate and washed with distilled water until the Hydrofilm layer dissolved. Then, the residual water was left to evaporate in a climatic chamber at 60 °C for 4 h and connected between two adhesive Cu electrodes. A customized pushing system was used to test the sensing capability of the 3D grids by providing vertical oscillations of the charged object. To investigate the sensing properties of the grid, polyethyleneterephthalate (PET) was set by rubbing against cotton (see the Supporting Information). The charged PET rod was put in oscillation between 3 and 1 cm from the 3D-printed grid. While the object oscillated, the open-circuit voltage values were recorded using a computer-controlled Keithley 4200 Source Meter Unit (Tektronix UK Ltd., The Capitol Building, Oldbury, UK). In the second case study, we considered the charge produced by fermenting beer yeast; *Saccharomyces cerevisiae*-based commercial beer yeast extract with additives was used as the medium for fermentation. A water solution (50 mg/mL) of yeast was prepared in a sterilized flask at 110 rpm and 30 °C for 1 h. After that, sugar (*i.e.*, sucrose) was added for the fermentation. The amount of sugar added is usually between three and five times the weight of the medium. Copper electrodes were applied to the wall of the PET vial and connected to the electrical measurement system.

The effect of human skin on the sensor was finally investigated: a hand was moved to 1 cm from the sample, and the voltage was recorded across the external load connected to the grid.

2.8. Statistical Analysis. GraphPad Prism 9.2.0.332 (GraphPad software, San Diego, CA) was used to assess the statistical significance of all comparison studies in this work. In the statistical analysis for comparison between multiple groups, a two-way ANOVA with Tukey's post hoc analysis (multiple comparisons) was conducted with the significance threshold of $*p < 0.05$, $**p \leq 0.01$, $***p \leq 0.001$, and $****p \leq 0.0001$. For cytotoxicity data, one-way ANOVA analysis was done and the significance threshold was $*p < 0.01$, $**p < 0.001$, and $***p < 0.0001$.

https://doi.org/10.1021/acsomega.2c04729
ACS Omega 2022, 7, 43729−43737

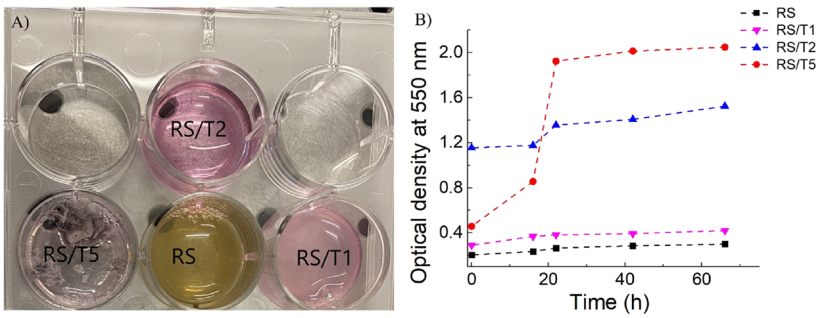

Figure 2. (A) Photograph of RS and RS/T gels. (B) Optical density changes (at 550 nm) of the RS and RS/T solutions as a function of time.

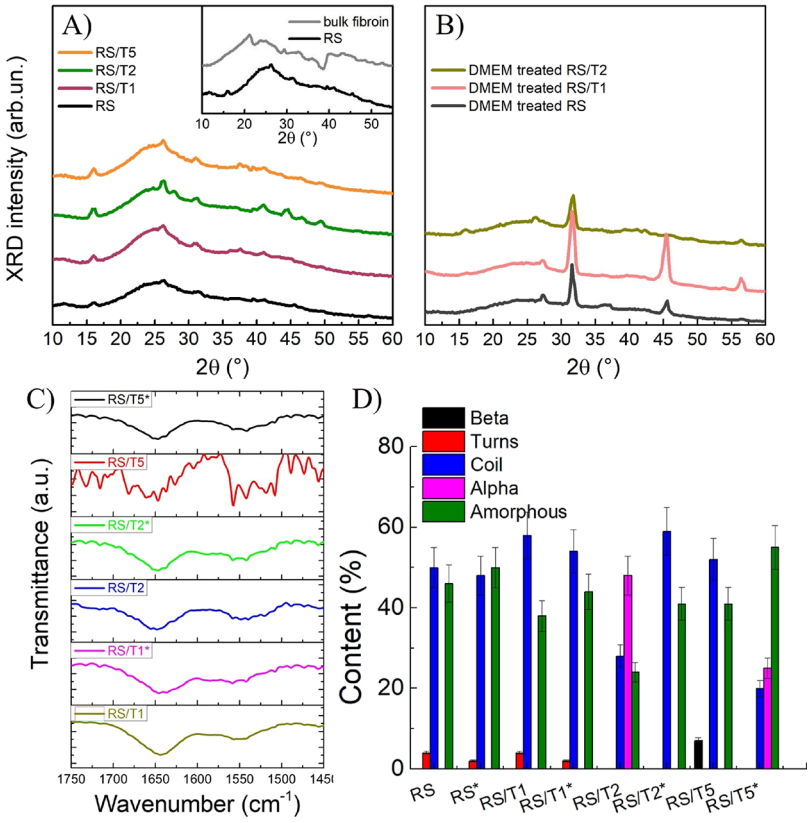

Figure 3. (A) XRD patterns for RS and RS/T samples for different weight concentrations of tannin regenerated in FA solution and (B) after the redispersion with DMEM. Inset of panel (A): XRD curves for bulk fibroin and RS. Curves are vertically shifted for clarity. (C) The asterisk indicates the FTIR spectra of neat RS and RS/T composites starting from the 60/40 composition obtained from FA solution and after redispersion in DMEM. (D) Structure composition of the prepared specimens with both procedures. The asterisks indicate the samples redispersed in DMEM.

3. RESULTS AND DISCUSSION

We considered the RS-based materials as structural and supporting substrates possessing ionic conductivity due to the presence of Ca^{2+} ions.[35] Hence, we focused on investigating the ionic conductive behavior of RS and RS/T samples. As reported in Figure 1A, when the Ca^{2+} mass ratio increases from 90/10 to 60/40, the conductivity of the RS increases. This increase in ionic conductivity relies on the content of both Ca^{2+} ions and trapped water in the final materials. Thus, we focus on the 60/40 composition for the subsequent investigation and 3D printing. As reported in Figure 1A, the conductivity of RS/T significantly increases also as a response to the presence of tannin. For example, when the tannin content passes from 1 to 5 wt %, the ionic conductivity increases by two orders of magnitude. Based on these experimental results, we can propose a similar model of the effect of tannin addition on the conductivity enhancement of polymer films;[36] a large number of hydroxyl groups on tannin provided opportunities for RS to interact with tannin through van der Waals forces (such as hydrogen bonding interactions). In contrast, the interactions between RS chains remain the same, which results in samples with higher conductivities.

The mutual interactions of ions, tannin, and silk fibroin are humidity-dependent, thus allowing the tuning of ionic conductivity. Indeed, as shown in Figure 1B, the current intensity of RS, RS/T1, and RS/T5 samples varies in step, with RH changes from 0 to 80%. Fitting the current−voltage curves and assuming valid Ohm law, current data can be converted to the conductivity change−RH curve as shown in Figure 1B. The slope of the linear region of the data reported in Figure 1B allows us to estimate the sensitivity value (*i.e.*, $\delta(\Delta S/S_0)/\Delta RH$, where ΔS, S_0, and ΔRH are the conductivity change, initial

https://doi.org/10.1021/acsomega.2c04729
ACS Omega 2022, 7, 43729−43737

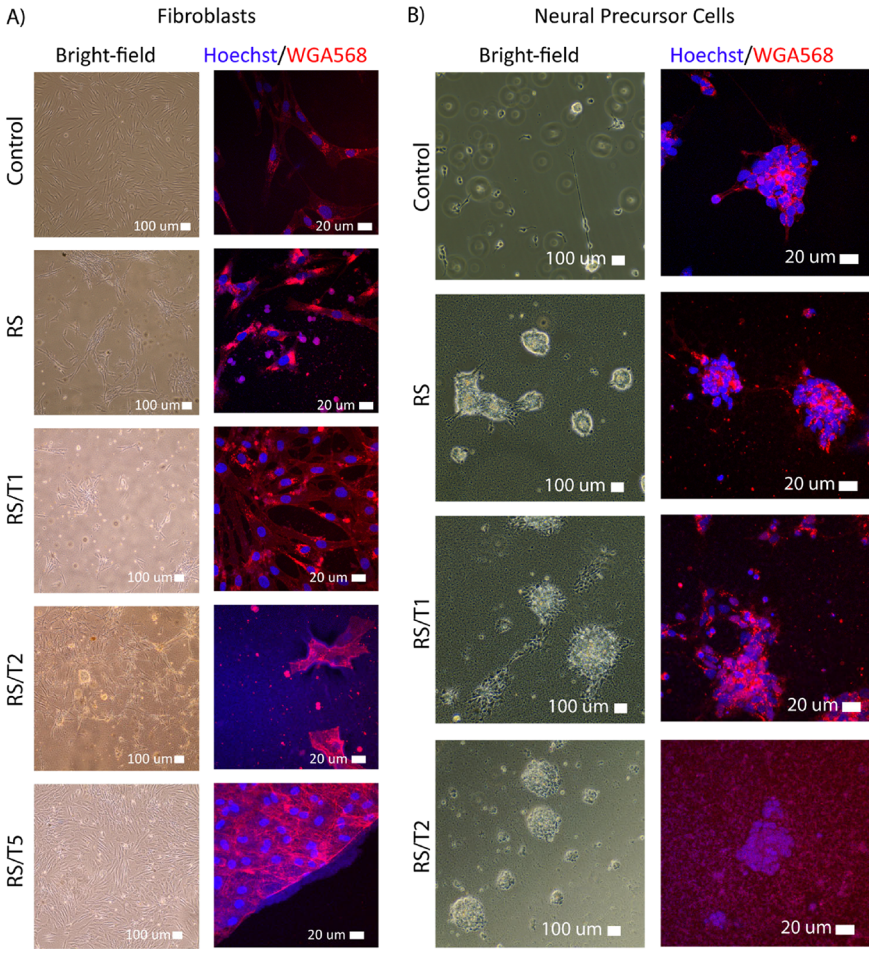

Figure 4. (A) Fibroblast and (B) NPC adhesion and growth on RS and RS/T hybrids. Bright-field (left) and confocal microscopy (right) images of human fibroblasts and NPCs seeded on modified glass surfaces covered with RS Hybrid films after 7 days of incubation in standard conditions. Cells were labeled with the fluorescent Hoechst (blue channel) and WGA568 (red channel) dyes, targeting DNA and sialic acid—component of the plasma membrane—respectively. Confocal images correspond to maximum intensity *Z* axis projections over 10 μm. Scale bars indicate 100 μm for bright-field microscopy and 20 μm for confocal microscopy.

conductivity, and RH change, respectively), which is 4.9% RH^{-1}. It should be observed that the conductivity of the RS/T5 sample exhibits a trend of decrease and then increase with increasing humidity values; this effect could be attributed to a slight swelling of the sample with increasing thickness as recently reported elsewhere.[33] We then examined the effect of temperature change from −15 to 25 °C on the 60/40 RS/T5 film (Figure 1C and Figure S1). The film shows evident conductivity variation amplitude in three cycles at these two temperatures.

By redispersing RS and RS/T samples in DMEM, the resulting material has the aspect of a gel (Figure 2A). Upon gelation, fibroin yielded an opaque color depending on the different compositions of the solutions. OD changes over time for RS and RS/T solutions are reported in Figure 2B. The observed OD changes are associated with the shift in the fibroin structure reported below. The OD increase observed with increasing tannin content up to 5 wt % suggests a saturation effect typical of gelation.[34] This behavior is less marked when lower tannin contents are used.

The XRD technique was used to characterize the crystalline structure of the prepared films. XRD patterns of RS in FA solution, after drying, and bulk silk fibroin are reported in the inset of Figure 3A. The regenerated silk exhibited a broad, amorphous peak centered at around $2\theta = 25°$, which mainly arises from the convolution of different bands at 19.4°, 20.3°, 24.6°, and 29.3°, corresponding to silk I crystalline spacing values of 0.44, 0.41, 0.35, and 0.30 nm, respectively, in agreement with literature data.[37−40] This pattern differs from bulk fibroin, mainly ascribed to the silk II crystalline structure. Formic acid dissolves silk, disrupting the hydrogen bonds within the antiparallel β-sheet structures. In RS, antiparallel β-structures are thus substituted by β-turns, which confer a different toughness to the silk fibers.

Moreover, superimposed on an amorphous silk band, a pattern of low-intensity Bragg peaks is visible, whose linewidth indicates the presence of crystals of micrometric size in the silk matrix. According to the literature, these crystals can be ascribed to a mixture of different hydrated forms of $CaCl_2$.[41] In particular, the peak at $2\theta = 16°$, not present in the XRD pattern of anhydrous $CaCl_2$, is a clear marker of the hydration of $CaCl_2$.

Samples obtained by adding tannin show a silk XRD curve with a broad band at $2\theta = 25°$, very similar to RS, proving that tannin preserves the crystalline structure of regenerated silk. However, Bragg peaks with different relative intensities can be observed in these samples, suggesting a different orientation of the corresponding $CaCl_2$ microcrystals. Although not very

https://doi.org/10.1021/acsomega.2c04729
ACS Omega 2022, 7, 43729−43737

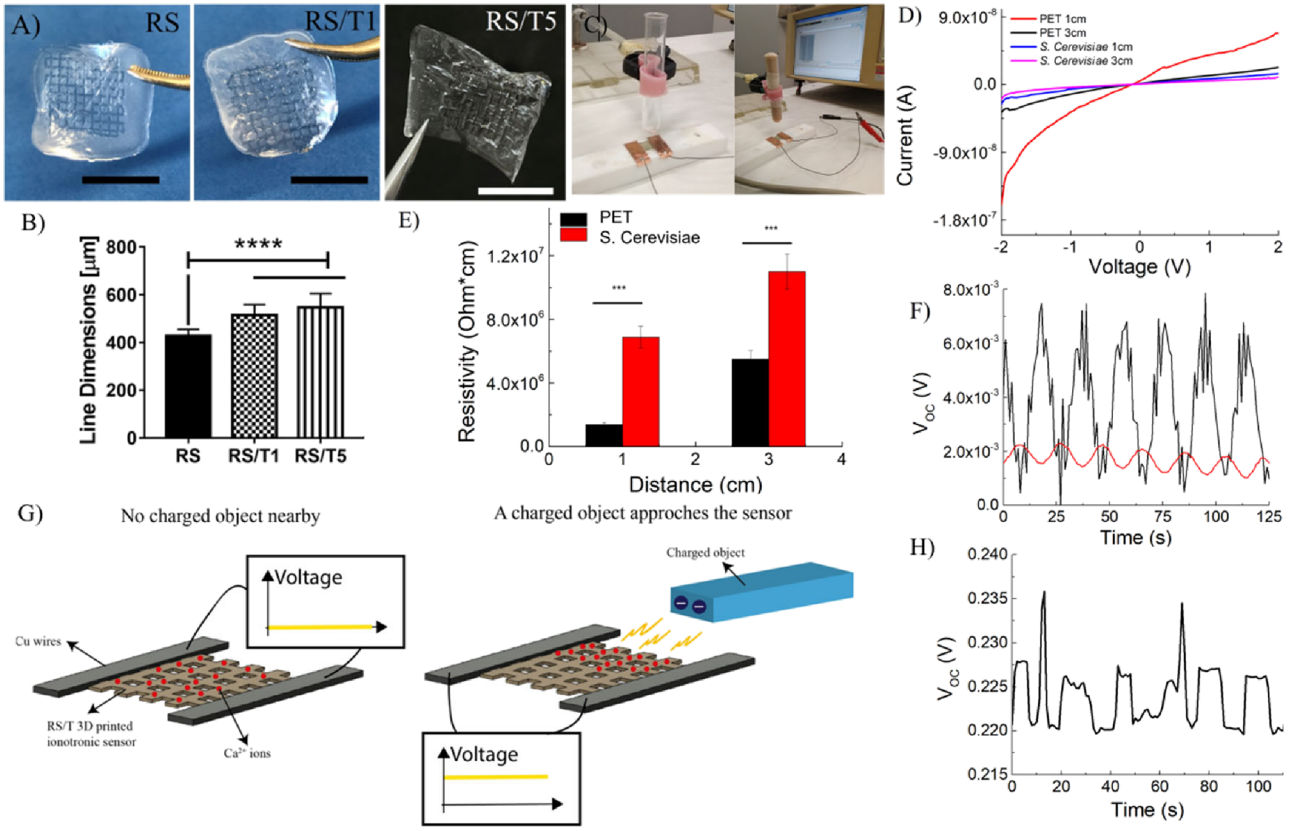

Figure 5. 3D-printed sensing grids based on the RS/T5 sample. (A) Photos of the structures of RS, RS/T1, and RS/T5 grids after the 3D printing process and acetate foil removal. The scale bars indicate 10 mm. (B) Linewidth for each RS-based solution. (C) Photographs showing the RS/T grid transferred on the Teflon substrate and PET and *S. cerevisiae* fermenting yeast objects positioned to a distance of 1 cm. The scale bar indicates 10 mm. (D) Current−voltage characteristics of charged PET and fermenting yeast placed at distances of 1 and 3 cm, respectively. (E) Electrical resistivity of the RS/T5 grid measured by positioning charged PET and fermenting yeast at distances of 1 and 3 cm, respectively. (F) The induced open-circuit voltage was measured, while the PET object's initial distance varied between the sample and the object. The red line indicates the oscillating length between 3 and 1 cm. (G) Scheme illustrating the sensing mechanism of the RS/T ionotronic sample; nearby things that usually have static charges on their surfaces cause the model to be charged through noncontact electrification, thus inducing a voltage change in the RS/T electric field receiver. (H) Graph of induced open-circuit voltage across the external load when the skin was used as a charged object (see Movie S1).

high, we also noted that the power of the Bragg peaks varies on repeated measurements of the same sample without a clear temporal trend (see Figure S2). We speculate that these variations can be ascribed to rearrangements on the micrometric scale, probably due to the modification of the sample hydration degree.

XRD curves relative to the samples after DMEM treatment are reported in Figure 3B for tannin at 0 wt %, RS/T1, and RS/T2. The silk II crystalline structure is preserved, but a different and more intense Bragg pattern, ascribed to the presence of microcrystals of varying composition and size, is observed. Also, in this case, XRD patterns of every sample slightly change with time: additional measurements performed by rotating the sample (data not shown) exhibit a complex and very intense pattern of several Bragg peaks, indicating that the microcrystals' positions and orientations change due to the mechanical micrometric movements and rearrangements of the gel form. Indeed, samples dissolved in DMEM, even after solvent evaporation, present a gel phase in which microcrystals may rearrange their orientation. Finally, from the XRD spectra, we did not record peaks related to the structure functions of liquid formic acid;[42] from this evidence, we can assume a negligible amount of residual formic acid in our samples.

Fourier transform infrared attenuated total reflection spectroscopy (FTIR-ATR) is a widely acknowledged method to investigate the chain conformation (*i.e.*, β-sheets, random coils, α-helices, and turns) of silk fibroin cast films.[30,43,44] The comparison of the FTIR spectra between new RS and RS/T samples and those dispersed in DMEM (Figure 3C and Figure S3) shows the signature bands associated with RS, such as amide I (1642 cm^{-1}) and amide II (1515 cm^{-1}), as previously reported.[30] The results reporting the secondary protein structure content are reported in Figure 3D. From these data, adding tannin to RS generally increased the amorphous structure when the RS/T samples were redispersed in DMEM.

MTT assay was performed on RS/T2 and RS/T5 samples. After 24 h, all the compounds with a concentration in the range of 7.8 μg/mL to 0.25 mg/mL resulted in safe results for the CaCo-2 cell line (see Figure S4); a very low cytotoxic effect (viability, <80%) was observed with RS/T5 at 0.5 mg/mL and with RS/T5 at the highest concentration (1 mg/mL). On the contrary, RS/T2 demonstrated safe results for all concentrations assayed. After 48 h of treatment, the highest concentration resulted in cytotoxicity for cells: 0.5 and 1 mg/mL. In particular, RS/T5 showed a viability <70% with 0.5 mg/mL and a viability around 60% with 1 mg/mL. The best result was obtained with RS/T2 with a safe profile after 24 h

https://doi.org/10.1021/acsomega.2c04729
ACS Omega 2022, 7, 43729−43737

(up to 1 mg/mL) and 48 h (up to 0.5 mg/mL). The bioresorbability of the RS and RS/T samples was also investigated (Figure S4). The RS sample largely dissolves within 4 days, with a difference for the RS/T samples that show degradation within 7 days.

Fibroblast and NPC morphology, confluence, and growth indicate the good biocompatibility of RS hybrids (Figure 4A,B). As described in the literature, we observed that low doses of tannin were not cytotoxic to fibroblasts[45] and NPCs, confirming their antioxidant and cytoprotective properties. In particular, tannin appears to positively influence fibroblast and NPC adhesion (Figure 4A,B) and fibroblast proliferation by the increase in cell confluence in Figure 4A. The cell viability assay was evaluated based on the ratio of live (>80%) and dead cells (automated cell counting by Trypan Blue Viability Assay) and based on the fibroblast and NPC morphology, growth, and confluence that were evaluated daily by an inverted microscope.

Then, we explored the capabilities of these biomaterials to be used as inks for extrusion-based 3D printing (Figure 5A). The involved solutions possess a liquid-like behavior, with G'' higher than G' for all the tested solutions, as we previously showed.[24] Moreover, they exhibit a Newtonian behavior, with a viscosity approximately equal to 4 mPa s and the absence of a yield stress. As clearly stated in the literature,[46,47] those rheological properties do not favor the printability of complex 3D shapes using the selected material. However, since the aim of this paper is the microfabrication of four-layer grids, the rheological properties should only favor the extrudability of the materials, granted by the low viscosity, and the shape retention, connected to the surface tension.

Indeed, the dimension of the grid lines depends on the interaction between the RS hybrid inks and the substrate. The final linewidth is larger than the needle size used for printing (*i.e.*, internal diameter of 210 μm) and increases with the content of tannins (428, 514, and 546 μm, respectively, for RS, RS/T1, and RS/T5) due to more pronounced surface wettability, as previously shown.[24] Statistical analysis revealed a significant difference ($p < 0.0001$) when the tannins were added to the solution regardless of the tannin concentration. In contrast, no significant differences arose between the grids made of different tannin-laden RS solutions (Figure 5B). Printing performance in terms of line dimensions could be improved in the future, taking into consideration the increase in line dimensions during the grid design and the printing parameter selection (*e.g.*, decreasing the volumetric flow). Thus, we will be able to fabricate grids with narrower line dimensions until the limit imposed by the Plateau−Rayleigh instability.[46]

Thanks to the design freedom given by 3D printing, we focused on holey structures, which provide several mechanical advantages compared with casted solid ones.[24] In particular, the decrease in the unwanted lateral displacement, global stiffness, and the stress of the single grid line allow the grids to more easily comply with movements and deformations of substrates on which they can be transferred to act as sensors.

The bioelectrical environment of the gut is regulated by the ionic conductance of live bacterial strains;[48] our 3D grid was utilized as a proof of concept to investigate the bioelectrical processes of a living yeast cell during its division (Figure 5C−E). Considering that this process occurs in the environment of the gut, we investigate the degradation in terms of weight loss of the prepared samples (Figure S5). From these results, we observed that tannin reduces the degradation. We choose the *S. cerevisiae* yeast cell because its genome is completely sequenced and not pathogens; therefore, it can be handled without precautions. The bioelectrical signal of *S. cerevisiae* was found to induce electrical resistivity variations by moving the vial between two fixed positions. These findings pave the way for using such 3D-printed materials to investigate the gut microenvironment. We also test the sensing capability of the RS/T5 grid of a charged object (*i.e.*, PET) that was fixed between two fixed distances (Figure 5C−E). When the charged object vertically oscillated, the induced voltage generated by the relative position was measured (Figure 5F). This effect can be explained based on electrostatic induction: when a charged object is approaching (Figure 5G), it originates an electric field that causes an electric current and potential drop across the external load between the receiver and the ground (Figure S6). Thus, by measuring the open-circuit voltage, we can estimate the intensity of the object's electric field and, as a consequence, its distance from the receiver. These findings prove the potentiality of the RS/T grid to detect a hand movement, thus catching skin as a charged object in a noncontact manner (Figure 5H and Movie S1).

4. CONCLUSIONS

Designing electronics exploiting the mechanisms of biological tissues and improving sensing with the surrounding environment is challenging mainly when turning toward using natural rather than synthetic materials. Silk fibroin is used in this context. In this study, we developed a novel ionotropic silk-based material that serves as a substrate for cell seeding and proliferation, mimicking the physiologically performed functions by the extracellular matrix as close as possible. We reported results showing that the hybrid silk formation can be applied as anchorage to many cell types, including fibroblasts and iPSc-derived neural precursor cells. It was demonstrated how adding tannin to the RS increases the ionic conductivity and allows the cells to migrate and connect. We demonstrated the use of silk fibroin in soluble plant-derived polyphenol as a biomaterial ink to prepare a 3D grid that senses an electric field originating from static charges on the surface of an object. We report a proof of concept on using these ionic sensors to detect the electrical amount produced by cell division by a non-invasive method. The results enlarged materials engineering, envisioning applications in noncontact sensors for implantable devices.

■ ASSOCIATED CONTENT

Data Availability Statement

Data can be made available upon reasonable request from the corresponding author.

Supporting Information

The Supporting Information is available free of charge at https://pubs.acs.org/doi/10.1021/acsomega.2c04729.

Current−voltage ($I-V$) curves recorded on the RS/T5 sample (Figure S1), XRD data of RS/T2 vs time (Figure S2), FTIR spectra on RS and RS* (Figure S3), MTT viability test on RS/T2 and RS/T5 samples after 24 and 48 h, respectively (Figure S4), weight loss of the prepared samples (Figure S5), and effects of a dielectric barrier and calculation of the charge from the equivalent circuit (Figure S6) (PDF)

https://doi.org/10.1021/acsomega.2c04729
ACS Omega 2022, 7, 43729−43737

Spatial perception of approaching skin (Movie S1) (MP4)

AUTHOR INFORMATION

Corresponding Author

Luca Valentini − *Civil and Environmental Engineering Department, University of Perugia, Terni 05100, Italy; Italian Consortium for Science and Technology of Materials (INSTM), Firenze 50121, Italy;* orcid.org/0000-0002-6803-5889; Email: luca.valentini@unipg.it

Authors

Irene Chiesa − *Department of Ingegneria dell'Informazione and Research Center E. Piaggio, University of Pisa, Pisa 56122, Italy*

Carmelo De Maria − *Department of Ingegneria dell'Informazione and Research Center E. Piaggio, University of Pisa, Pisa 56122, Italy;* orcid.org/0000-0002-1368-3571

Rodolfo Tonin − *Molecular and Cell Biology Laboratory, Paediatric Neurology Unit and Laboratories, Neuroscience Department, Meyer Children's Hospital, Firenze 50121, Italy;* orcid.org/0000-0002-2031-1530

Francesca Ripanti − *Department Physics and Geology, University of Perugia, 06123 Perugia, Italy*

Maria Rachele Ceccarini − *Department of Pharmaceutical Sciences, University of Perugia, 06123 Perugia, Italy*

Carlotta Salvatori − *Department of Ingegneria dell'Informazione and Research Center E. Piaggio, University of Pisa, Pisa 56122, Italy*

Lorenzo Mussolin − *Department Physics and Geology, University of Perugia, 06123 Perugia, Italy*

Alessandro Paciaroni − *Department Physics and Geology, University of Perugia, 06123 Perugia, Italy*

Caterina Petrillo − *Department Physics and Geology, University of Perugia, 06123 Perugia, Italy; AREA Science Park, 34149 Trieste, Italy*

Emanuele Cesprini − *Land Environment Agriculture & Forestry Department, University of Padua, 35020 Legnaro, Italy*

Federica Feo − *Molecular and Cell Biology Laboratory, Paediatric Neurology Unit and Laboratories, Neuroscience Department, Meyer Children's Hospital, Firenze 50121, Italy*

Martino Calamai − *European Laboratory for Non-linear Spectroscopy (LENS), University of Florence, Sesto Fiorentino 50019, Italy; National Institute of Optics−National Research Council (CNR-INO), Sesto Fiorentino 50019, Italy;* orcid.org/0000-0002-4031-7235

Amelia Morrone − *Molecular and Cell Biology Laboratory, Paediatric Neurology Unit and Laboratories, Neuroscience Department, Meyer Children's Hospital, Firenze 50121, Italy; Dipartimento Neuroscienze, Psicologia, Area del Farmaco e della Salute del Bambino NEUROFARBA, Università degli Studi di Firenze, Firenze 50121, Italy*

Antonino Morabito − *Dipartimento Neuroscienze, Psicologia, Area del Farmaco e della Salute del Bambino NEUROFARBA, Università degli Studi di Firenze, Firenze 50121, Italy; Department of Pediatric Surgery, Meyer Children's Hospital, Firenze 50139, Italy;* orcid.org/0000-0002-5323-3620

Tommaso Beccari − *Department of Pharmaceutical Sciences, University of Perugia, 06123 Perugia, Italy*

Complete contact information is available at: https://pubs.acs.org/10.1021/acsomega.2c04729

Author Contributions

The manuscript was written with contributions of all authors. All authors have approved the final version of the manuscript. I.C., F.R., M.R.C., C.S., L.M., R.T., F.F., M.C., E.C., and L.V. were involved in laboratory research. C.D.M., A.P., L.C., A.M., A.M., T.B., and L.V. wrote the original draft. L.V. contributed to the conceptualization of experiments and the overall coordination of the research activities.

Funding

L.V., I.C., and C.D.M. received funding from the Italian Ministry of Education, University and Research (MIUR) under the PRIN Project "Development and promotion of the Levulinic acid and Carboxylate platforms by the formulation of novel and advanced PHA-based biomaterials and their exploitation for 3D printed green-electronics applications" grant 2017FWC3WC. M.C. acknowledges funding from Laserlab-Europe, H2020 EC-GA 654148. Fondazione Cassa di Risparmio di Terni partially funded this work through the research grant 2020.

Notes

The authors declare no competing financial interest.
All photos/artworks used in the figures, including the TOC graphic, are original work and are not taken from another source.

ACKNOWLEDGMENTS

I.C. and C.D.M. acknowledge the support of the Crosslab Additive Manufacturing of the Department of Information Engineering of the University of Pisa. Prof. Gianluca Tondi, Department of Land Environment Agriculture and Forestry, University of Padua, is kindly acknowledged for supplying chestnut tannin.

REFERENCES

(1) Kalmijn, A. J. Electric and Magnetic Field Detection in Elasmobranch Fishes. *Science* **1982**, *218*, 916−918.

(2) Bellono, N. W.; Leitch, D. B.; Julius, D. Molecular Basis of Ancestral Vertebrate Electroreception. *Nature* **2017**, *543*, 391−396.

(3) Kramer, B. *Electroreception and Communication in Fishes* (Gustav Fischer, 1996), vol. *42*.

(4) Odent, J.; Wallin, T. J.; Pan, W.; Kruemplestaedter, K.; Shepherd, R. F.; Giannelis, E. P. Highly Elastic, Transparent, and Conductive 3D-Printed Ionic Composite Hydrogels. *Adv. Funct. Mater.* **2017**, *27*, 1701807.

(5) Lee, Y.; Song, W. J.; Jung, Y.; Yoo, H.; Kim, M.-Y.; Kim, H.-Y.; Sun, J.-Y. Ionic Spiderwebs. *Sci. Robot.* **2020**, *5*, eaaz5405.

(6) Lee, Y.; Cha, S. H.; Kim, Y.-W.; Choi, D.; Sun, J.-Y. Transparent and Attachable Ionic Communicators Based on Self-Cleanable Triboelectric Nanogenerators. *Nat. Commun.* **2018**, *9*, 1804.

(7) Zhu, B.; Wang, H.; Leow, W. R.; Cai, Y.; Loh, X. J.; Han, M.; Chen, X. Silk Fibroin for Flexible Electronic Devices. *Adv. Mater.* **2016**, *28*, 4250−4265.

(8) Ling, S.; Kaplan, D. L.; Buehler, M. J. Nanofibrils in Nature and Materials Engineering. *Nat. Rev. Mater.* **2018**, *3*, 18016.

(9) Ling, S.; Chen, W.; Fan, Y.; Zheng, K.; Jin, K.; Yu, H.; Buehler, M. J.; Kaplan, D. L. Biopolymer Nanofibrils: Structure, Modeling, Preparation, and Applications. *Prog. Polym. Sci.* **2018**, *85*, 1−56.

(10) Wang, L.; Guo, J.; Zhou, L.; Ye, C.; Omenetto, F. G.; Kaplan, D. L.; Ling, S. Design, Fabrication, and Function of Silk-Based Nanomaterials. *Adv. Funct. Mater.* **2018**, *28*, 1805305.

(11) Katz, A. K.; Glusker, J. P.; Beebe, S. A.; Bock, C. W. Calcium Ion Coordination: A Comparison with That of Beryllium, Magnesium, and Zinc. *J. Am. Chem. Soc.* **1996**, *118*, 5752−5763.
(12) Strynadka, N. C. J.; James, M. N. G. Crystal Structures of the Helix-Loop-Helix Calcium-Binding Proteins. *Annu. Rev. Biochem.* **1989**, *58*, 951−999.
(13) Shirmohammadli, Y.; Efhamisisi, D.; Pizzi, A. Tannins as a sustainable raw material for green chemistry: A review. *Ind. Crops Prod.* **2018**, *126*, 316−332.
(14) Ghahri, S.; Chen, X.; Pizzi, A.; Hajihassani, R.; Papadopoulos, A. N. Natural Tannins as New Cross-linking Materials for Soy-Based Adhesives Natural Tannins as New Cross-linking Materials for Soy-Based Adhesives. *Polymer* **2021**, *13*, 595.
(15) Pizzi, A. Tannins: Prospectives and actual industrial applications. *Biomolecules* **2019**, *9*, 344.
(16) Cesprini, E.; De Iseppi, A.; Giovando, S.; Tarabra, E.; Zanetti, M.; Šket, P.; Marangon, M.; Tondi, G. Chemical characterization of cherry (Prunus avium) extract in comparison with commercial mimosa and chestnut tannins. *Wood Sci. Technol.* **2022**, *56*, 1455−1473.
(17) Vishtal, A.; Kraslawski, A. Challenges in industrial applications of technical lignins. *BioResources* **2011**, *6*, 3547−3568.
(18) Yoo, C. G.; Ragauskas, A. J. Opportunities and Challenges of Lignin Utilization. *ACS Symp. Ser.* **2021**, *1377*, 1−12.
(19) Bai, S.; Zhang, X.; Cai, P.; Huang, X.; Huang, Y.; Liu, R.; Zhang, M.; Song, J.; Chen, X.; Yang, H. A Silk-Based Sealant with Tough Adhesion for Instant Hemostasis of Bleeding Tissues. *Nanoscale Horiz.* **2019**, *4*, 1333−1341.
(20) Deng, Z.; Wang, H.; Ma, P. X.; Guo, B. Self-healing conductive hydrogels: preparation, properties and applications. *Nanoscale* **2020**, *12*, 1224−1246.
(21) Deng, Z.; Hu, T.; He, J.; Ma, P. X.; Guo, B. Stimuli-responsive conductive nanocomposite hydrogels with high stretchability, self-healing, adhesiveness, and 3d printability for human motion sensing. *ACS Appl. Mater. Interfaces* **2019**, *11*, 6796−6808.
(22) Deng, Z.; Rui, Y.; Guo, B. Stimuli-responsive conductive hydrogels: design, properties, and applications. *Mater. Chem. Front.* **2021**, *5*, 2092−2123.
(23) Valentini, L.; Ceccarini, M. R.; Verdejo, R.; Tondi, G.; Beccari, T. Stretchable, Bio-Compatible, Antioxidant and Self-powering Adhesives from Soluble Silk Fibroin and Vegetal Polyphenols Exfoliated Graphite. *Nanomaterials* **2021**, *11*, 2352.
(24) Chiesa, I.; De Maria, C.; Ceccarini, M. R.; Mussolin, L.; Coletta, R.; Morabito, A.; Tonin, R.; Calamai, M.; Morrone, A.; Beccari, T.; Valentini, L. 3D Printing Silk-Based Bioresorbable Piezoelectric Self-Adhesive Holey Structures For *In Vivo* Monitoring On Soft Tissues. *ACS Appl. Mater. Interfaces* **2022**, *14*, 19253−19264.
(25) Cruz-Acuña, R.; García, A. J. Synthetic Hydrogels Mimicking Basement Membrane Matrices to Promote Cell-Matrix Interactions. *Matrix Biol.* **2017**, *57*−*58*, 324−333.
(26) Polykandriotis, E.; Arkudas, A.; Horch, R. E.; Kneser, U.; Mitchell, G. To Matrigel or Not to Matrigel. *Am. J. Pathol.* **2008**, *172*, 1441−1442.
(27) Kleinman, H. K.; Martin, G. R. Matrigel: Basement Membrane Matrix with Biological Activity. *Semin. Cancer Biol.* **2005**, *15*, 378−386.
(28) Josberger, E. E.; Hassanzadeh, P.; Deng, Y.; Sohn, J.; Rego, M. J.; Amemiya, C. T.; Rolandi, M. Proton Conductivity in Ampullae of *Lorenzini* Jelly. *Sci. Adv.* **2016**, *2*, e1600112.
(29) Hu, X.; Kaplan, D. L.; Cebe, P. Determining Beta-Sheet Crystallinity in Fibrous Proteins by Thermal Analysis and Infrared Spectroscopy. *Macromolecules* **2006**, *39*, 6161−6170.
(30) De Maria, C.; Chiesa, I.; Morselli, D.; Ceccarini, M. R.; Bittolo Bon, S.; Degli Esposti, M.; Fabbri, P.; Morabito, A.; Beccari, T.; Valentini, L. Biomimetic Tendrils by 4D-printing Bimorph Springs with Torsion and Contraction Properties Based on Bio-compatible Graphene/Silk Fibroin and Poly(3-Hydroxybutyrate-Co-3-Hydroxyvalerate). *Adv. Funct. Mater.* **2021**, *31*, 2105665.
(31) Pagano, C.; Perioli, L.; Latterini, L.; Nocchetti, M.; Ceccarini, M. R.; Marani, M.; Ramella, D.; Ricci, M. Folic Acid-layered Double Hydroxides Hybrids in Skin Formulations: Technological, Photochemical and *In Vitro* Cytotoxicity on Human Keratinocytes and Fibroblasts. *Appl. Clay Sci.* **2019**, *168*, 382−395.
(32) Zheng, Y.; Wang, L.; Zhao, L.; Wang, D.; Xu, H.; Wang, K.; Han, W. A flexible humidity sensor based on natural biocompatible silk fibroin films. *Adv. Mater. Technol.* **2021**, *6*, 2001053.
(33) Matsumoto, A.; Chen, J.; Collette, A. L.; Kim, U.-J.; Altman, G. H.; Cebe, P.; Kaplan, D. L. Mechanisms of Silk Fibroin Sol-Gel Transitions. *J. Phys. Chem. B* **2006**, *110*, 21630−21638.
(34) Ling, S.; Zhang, Q.; Kaplan, D. L.; Omenetto, F.; Buehler, M. J.; Qin, Z. Printing of stretchable silk membranes for strain measurements. *Lab-on-a-Chip* **2016**, *16*, 2459−2466.
(35) Yi, Z.; Zhao, Y.; Li, P.; Ho, K.; Blozowski, N.; Walker, G.; Jaffer, S.; Tjong, J.; Sain, M.; Lu, Z. The effect of tannic acids on the electrical conductivity of PEDOT:PSS films. *Appl. Surf. Sci.* **2018**, *448*, 583−588.
(36) Um, I. C.; Kweon, H.; Park, Y. H.; Hudson, S. Structural characteristics and properties of the regenerated silk fibroin prepared from formic acid. *Int. J. Biol. Macromol.* **2001**, *29*, 91−97.
(37) Zhang, H.; Li, L. L.; Dai, F. Y.; Zhang, H. H.; Ni, B.; Zhou, W.; Yang, X.; Wu, Y. Z. Preparation and characterization of silk fibroin as a biomaterial with potential for drug delivery. *J. Transl. Med.* **2012**, *10*, 117.
(38) Kamalha, E.; Zheng, Y. S.; Zeng, Y. C.; Fredrick, M. N. FTIR and WAXD Study of Regenerated Silk Fibroin. *Adv. Mater. Res.* **2013**, *677*, 211−215.
(39) Jaramillo-Quiceno, N.; Álvarez-López, C.; Restrepo-Osorio, A. Structural and thermal properties of silk fibroin films obtained from cocoon and waste silk fibers as raw materials. *Procedia Eng.* **2017**, *200*, 384−388.
(40) Karunadasa, K. S.; Manoratne, C. H.; Pitawala, H. M. T. G. A.; Rajapakse, R. M. G. Relative stability of hydrated/anhydrous products of calcium chloride during complete dehydration as examined by high-temperature X-ray powder diffraction. *J. Phys. Chem. Solids* **2018**, *120*, 167−172.
(41) Jedlovszky, P.; Bakó, I.; Pálinkás, G.; Dore, J. C. Structural investigation of liquid formic acid. *Molecular Physics: An International Journal at the Interface Between Chemistry and Physics* **1995**, *86*, 87−105.
(42) Tretinnikov, O. N.; Tamada, Y. Influence of casting temperature on the near-surface structure and wettability of cast silk fibroin films. *Langmuir* **2001**, *17*, 7406−7413.
(43) Teramoto, H.; Miyazawa, M. Molecular orientation behavior of silk sericin film as revealed by ATR infrared spectroscopy. *Biomacromolecules* **2005**, *6*, 2049−2057.
(44) Khan, N. S.; Ahmad, A.; Hadi, S. M. Anti-Oxidant, Pro-oxidant properties of tannic acid and its binding to DNA. *Chem.-Biol. Interact.* **2000**, *125*, 177−189.
(45) Bonatti, A. F.; Chiesa, I.; Vozzi, G.; De Maria, C. Open-source cad-cam simulator of the extrusion-based bioprinting process. *Bioprinting* **2021**, *24*, e00172.
(46) Paxton, N.; Smolan, W.; Böck, T.; Melchels, F.; Groll, J.; Jungst, T. Proposal to assess printability of bioinks for extrusion-based bioprinting and evaluation of rheological properties governing bioprintability. *Biofabrication* **2017**, *9*, 044107.
(47) Cremin, K.; Jones, B. A.; Teahan, J.; Meloni, G. N.; Perry, D.; Zerfass, C.; Asally, M.; Soyer, O. S.; Unwin, P. R. Scanning Ion Conductance Microscopy Reveals Differences in the Ionic Environments of Gram-Positive and Negative Bacteria. *Anal. Chem.* **2020**, *92*, 16024−16032.

https://doi.org/10.1021/acsomega.2c04729
ACS Omega 2022, 7, 43729−43737